International Journal of Precision Engineering and Manufacturing-Green Technology
https://doi.org/10.1007/s40684-024-00653-5

Online ISSN 2198-0810
Print ISSN 2288-6206

REGULAR PAPER

Integration of Cu-Doped TiO_2 Nanoparticles on High Surface UV-Laser-Induced Graphene for Enhanced Photodegradation, De-icing, and Anti-bacterial Surface Applications

Jun Uk Lee[1] · Bo-Seok Kang[2] · Yong-Won Ma[3] · Rafaela Aguiar[1] · Bo-Sung Shin[4] · Patrick C. Lee[1]

Received: 20 January 2024 / Revised: 4 July 2024 / Accepted: 23 July 2024

Abstract
The increasing demand for versatile graphene-based materials, incorporating semimetal nanoparticles (NPs), is driving contemporary societies towards platforms that harness solar radiation for biocidal activity, de-icing, and photodegradation. This study investigates the photoinduced antibacterial activity, de-icing, and photocatalytic properties of Cu-doped TiO_2/Ultraviolet (UV)-Laser-Induced Graphene (LIG). Cu-doped TiO_2/UV-LIG exhibits considerable promise when subjected to solar radiation, particularly in applications such as de-icing, photodegradation and antibacterial efficacy. Characterized by nanopores and a surface area of 396 m^2/g, Cu-doped TiO_2/UV-LIG achieved a noteworthy temperature of 91.7°C under 1 SUN irradiance, thus establishing a significant milestone in the field of LIG. Initially, it demonstrated exceptional phenol degradation efficiency at 86%, and this efficiency remained noteworthy at 83% even after undergoing five cycles of use, thus emphasizing its enduring degradation capacity. Moreover, at 0.5 SUN intensity, it demonstrated remarkable efficacy in eradicating over 99.999% of foodborne pathogens.

Keywords Laser-induced graphene · TiO_2 · Foodborne pathogen · De-icing · Photodegradation · Antibacterial

1 Introduction

Semiconductor nanoparticles (NPs) hold great promise for driving light-induced processes like solar fuel generation, photocatalytic pollutant remediation, and converting solar energy into electricity [1–3]. Harnessing these materials alongside light offers a pathway to reduce reliance on fossil fuels and address pressing environmental challenges [4]. However, the persistent challenge of severe recombination of photogenerated charge carriers, especially in semiconductors with multiple cations, remains a significant bottleneck [4, 5]. This issue often results in shortened lifetimes of photoexcited electrons and holes, leading to reduced quantum efficiency in various light-driven applications. Conversely, the combination of semiconducting oxides with laser-induced graphene (LIG) has garnered significant interest recently [6–9]. This is partly due to LIG's ability to enhance charge separation and transport through its honeycomb sp2 network structure. Because of their large surface area and distinctive characteristics, these materials are ideal for uses like photothermal heating and solar-triggered photocatalysis; furthermore, LIG exhibits outstanding anti-biofouling properties and has been utilized in antibacterial devices activated through electrothermal or photothermal means. [10–12]. The bactericidal and photothermal heating capabilities of LIG can be improved by embedding semimetal NPs in the graphene sheets of LIG surface to form an interconnected open-cell network [13–15]. Ultraviolet (UV) lasers can be

Jun Uk Lee and Bo-Seok Kang have contributed equally to this work.

✉ Bo-Sung Shin
bosung@pusan.ac.kr

✉ Patrick C. Lee
patricklee@mie.utoronto.ca

[1] Multifunctional Composites Manufacturing Laboratory (MCML), Department of Mechanical and Industrial Engineering, University of Toronto, Toronto M5S 3G8, Canada

[2] Department of Cogno-Mechatronics Engineering, Pusan National University, Pusan, South Korea

[3] Interdisciplinary Department for Innovative Manufacturing Engineering, Pusan National University, Pusan, South Korea

[4] Department of Optics and Mechatronics Engineering, Pusan National University, Pusan, South Korea

Published online: 04 September 2024

used to create fine and precise graphene patterns with a high surface area and form metal oxide nanoparticles (MONPs) on the surface. UV-LIGs, as compared with traditional LIGs produced using visible or infrared lasers, offer several advantages and unique properties, including reduced thermal damage to the substrate or target material [16–18].

In this context, high-surface area Cu-doped TiO_2/UV-LIG exhibiting an excellent photo-based antibacterial performance was synthesized using UV-pulsed laser. Titanium dioxide (TiO_2), a semiconductor material, exhibits photocatalytic activity under UV light, and the addition of Cu enhances antibacterial and photocatalytic properties. Therefore, the bimetallic Cu-doped TiO_2 materials produced in this study exhibited an outstanding photocatalytic performance [19, 20]. Furthermore, the incorporation of large surface area graphene extends the light absorption range of traditional TiO_2 photocatalysts, allowing them to respond to both UV and visible light [21, 22]. The photodegradation, de-icing, and antibacterial efficacy of the prepared Cu-doped TiO_2/UV-LIGs with different surface areas were thoroughly assessed under simulated solar irradiation.

2 Materials and Methods

2.1 Materials

All reagents were obtained from commercial suppliers and used without further purification. A 125-μm thick commercial PI film was provided by DuPont™ Wilmington (Wilmington, DE, USA). $CuCl_2$ and $TiCl_4$ solutions (1 wt. %) were obtained from Sigma-Aldrich (St. Louis, MO, USA). The laser beam was delivered using a Galvano scanner (HurrySCAN III 14, SCANLAB, Pucheim, Germany) and an F-θ lens with a 105.9 mm focal length (S4LFT4100/075 Telecentric Scan Lens, Sill Optics GmbH, Wendelstein, Germany). Table S1 (Online Resource 1) provides the Galvano scanner specifications.

2.2 Fabrication of the Cu-Doped TiO_2/UV-LIG Composite Films

Figure 1 schematically depicts the Cu-doped TiO_2/UV-LIG composite preparation process. Figure S1 (Online Resource 1) shows photographic images and a diagram of the customized pulsed laser system operating at a wavelength of 355 nm. Table S2 (Online Resource 1) lists the specifications of the 355 nm UV pulsed laser. The Cu-doped TiO_2/UV-LIG composite films were fabricated using a unidirectional laser processing strategy, as shown in Fig. 1a. An initial laser irradiation, set at a power of 1.2 W and scanning speed of 60 mm s^{-1}, at room temperature (approximately 23–25 °C) was employed to create a hydrophilic and porous pattern on the LIG surface, as depicted in Fig. 1b. Subsequently, the UV-LIG surface was treated with 2.5 μL of 1 M $CuCl_2$ and 5 μL of 1 M $TiCl_4$, as illustrated in Fig. 1c. A second UV laser irradiation on the metal chloride solution-coated UV-LIG substrate can induce the hydrothermal synthesis of MONPs [23, 24]. Copper-doped TiO_2 NPs were uniformly dispersed on the UV-LIG using secondary laser irradiation. The dynamic fluence and overlapping factor (O_f), which regulate the UV-LIG shape as well as the distribution and size of NPs, can be easily controlled by adjusting the laser scanning speed. Table S3 (Online Resource 1) lists the laser beam conditions used to fabricate the Cu-doped TiO_2 /UV-LIG samples. To examine the changes in the shape and chemistry of the Cu-doped TiO_2/UV-LIG influenced by the dynamic fluence and O_f, the samples were categorized into three types according to their corresponding dynamic fluence, namely, low fluence (13 J/cm^2 at 100 mm s^{-1}), medium fluence (21.66 J/cm^2 at 60 mm s^{-1}), and high fluence (65 J/cm^2 at 20 mm s^{-1}) samples. Figure 1d shows a diagram showing the Cu-doped TiO2 NPs/UV-LIG with antimicrobial properties based on synergistic effect including graphene edge, photothermal heating and reactive oxygen species (ROS).

2.3 Characterizations

The morphologies of the Cu-doped TiO_2/UV-LIG samples were examined using field-emission scanning electron microscopy (FE-SEM; TESCAN MIRA 3 LMH In-Beam detector, Brno, Czech Republic). The compositions and chemical bond states of the Cu-doped TiO_2/UV-LIG samples were analyzed using X-ray photoelectron spectroscopy (XPS; Multilab 2000, THERMO VG SCIENTIFIC, Waltham, MA, USA.) A Raman spectrometer (NRS-5100, JASCO International Co., Ltd., Tokyo, Japan), employing a 532-nm excitation line, was used to further confirm the formation of the Cu-doped TiO_2/UV-LIG composites and characterize their properties. The surface areas and pore sizes of the samples were quantified using an Autosorb IQ instrument (Quantachrome, Boynton Beach, FL, USA).

2.4 Photodegradation Experiments

A primary 1000 ppm-concentration solution was carefully prepared by dissolving 1 g phenol (Sigma-Aldrich, purity 99%) in 1 L distilled water. This solution was stored in a light-impervious desiccated environment to prevent any unintended reactions that could compromise its concentration. Subsequently, a synthetic wastewater solution was produced by diluting the phenol stock solution with distilled water to achieve the desired concentration. The pH of this solution was adjusted using diluted sulfuric acid or sodium hydroxide solutions. The resulting solution

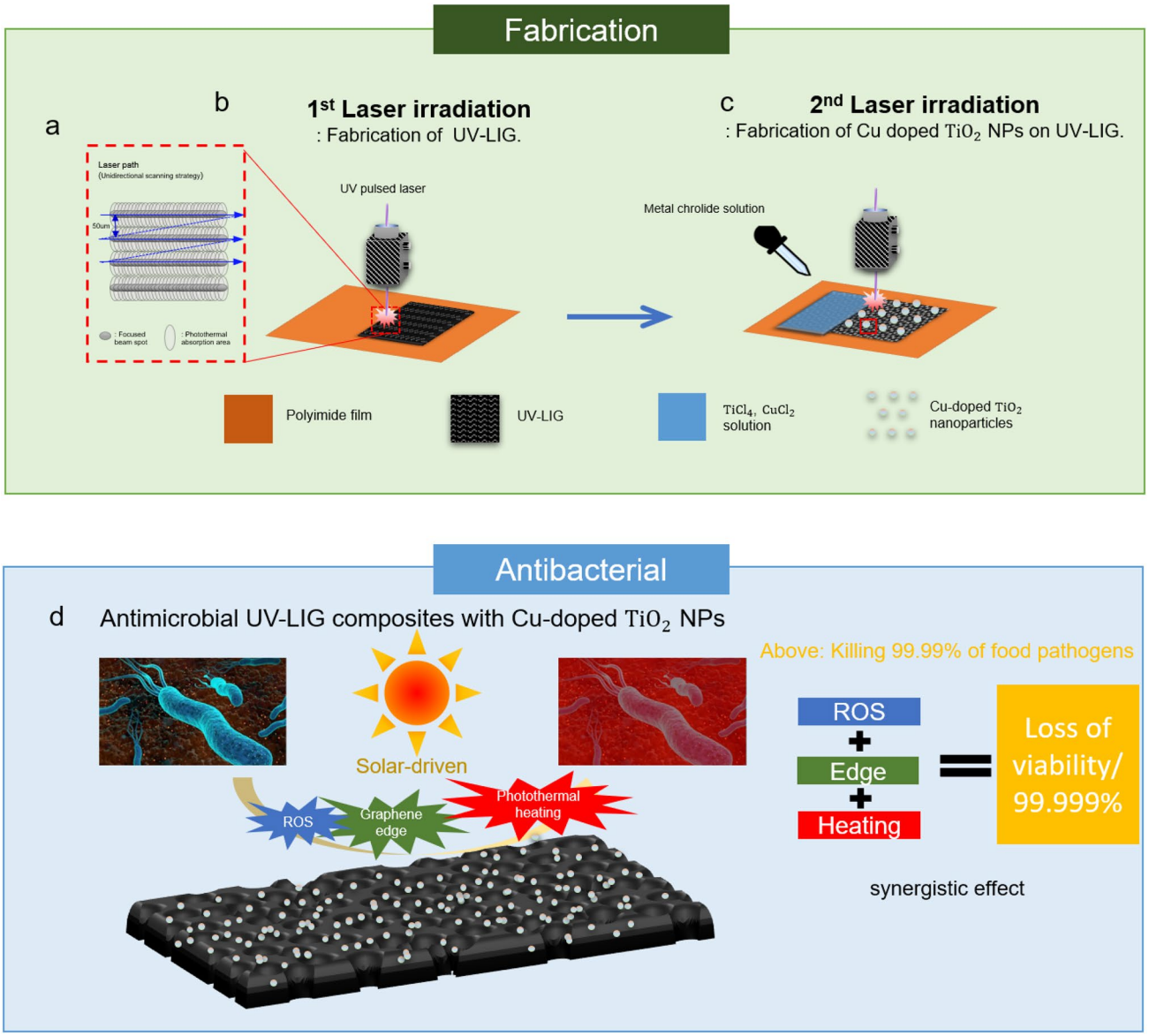

Fig. 1 Fabrication process of the Cu-doped TiO_2/UV-LIG composites: **a** schematic illustrating the laser pulse spot, **b** first irradiation of the PI film to produce porous UV-LIG, **c** second laser irradiation with $TiCl_4$ and $CuCl_2$ solutions on UV-LIG for the fabrication of Cu-doped TiO_2 NPs, and **d** schematic illustration of the antimicrobial UV-LIG composites containing Cu-doped TiO_2 NPs

was introduced into the reactor, where a specific mass of the photocatalyst was incorporated. Samples (4 mL) were extracted at regular intervals of 30 min for subsequent analysis. All samples underwent a 15-min centrifugation process prior to analysis using a tabletop centrifuge (DAIGGER) to separate the suspended catalyst. A 2.5 mL aliquot of the centrifuged sample was subjected to further analysis. The photodegradation efficacy was further assessed using a high-performance liquid chromatography (HPLC) system employing a ZORBAX 300SB-C18 (4.6 mm × 250 mm × 5 µm) column. The phenol removal efficiency under a solar simulator was determined by evaluating the phenol peak area obtained from the HPLC data using Eq. (1):

$$\textit{Phenol degradation efficiency}\ (\%) = \left(1-\frac{C_t}{C_0}\right)100 \qquad (1)$$

where C_0 and C_t denote the initial concentration of phenol and its concentration after time t during the catalytic reaction, respectively.

2.5 Bacterial Cultures

E. coli (O157:H7), *B. cereus* (NCTC 7464), and *S. typhimurium* (ATCC 14028) were acquired from the National Collection of Type Cultures (Colindale, London, UK) and the American Type Culture Collection (Manassas, VA, USA), respectively. These strains were stored in 30% (w/v) glycerol (Fisher Scientific, Itasca, IL, USA) at –80 °C. Subsequently, the *E. coli*, *B. cereus*, and *S. typhimurium* cultures were streaked and incubated for 24 h at 37 °C on tryptic soy agar (TSA, Difco, Detroit, MI, USA). Single colonies of each bacterium were then transferred to 50 mL tubes containing 30 mL tryptic soy broth (Difco, Detroit, MI, USA) and incubated overnight at 37 °C under shaking at 150 rpm. Each incubated cultured cell suspension was centrifuged at 4000 rpm for 10 min at 4 °C and washed twice using a sterile 0.85% saline solution to obtain purified cell pellets. The resulting cell pellets were resuspended and diluted to approximately 7 log CFU/mL in a sterile 0.85% saline solution, which served as the inoculum solution for subsequent experiments.

2.6 Treatment of Foodborne Pathogens Using the Cu-Doped UV-LIG Composite Films

The three Cu-doped UV-LIG composite films were treated using an inoculum solution of *E. coli*, *B. cereus*, and *S. typhimurium* to evaluate their inactivation effect on foodborne pathogens. A 100 µL aliquot of each inoculum solution was applied to the prepared LIG film surfaces (1 cm × 1 cm) and exposed to 0.5 SUN for durations of 1 min and 5 min. An inoculum solution without the Cu-doped TiO_2/UV-LIG composite film treatment was used as the control.

2.7 Microbiological Analysis

After treatment with the MONP-LIG composite films, the inoculum was transferred to a sterile glass test tube for recovery. Each recovered inoculum solution was serially diluted using sterile 0.85% saline. The microbial counts for *E. coli* and B. *cereus* and for *S. typhimurium* were determined using mannitol egg yolk polymyxin (MYP; Oxoid, Basingstoke, Hampshire, UK) and xylose lysine deoxycholate agar (XLD; Difco Laboratories, Detroit, MI, USA), respectively. The MYP and XLD plates were incubated at 37 °C for 24 h. Each microbial count was performed in triplicate and expressed as log CFU/mL.

2.8 Statistical Analysis

All experiments were conducted thrice using a completely randomized factorial experimental design. The results are presented as a mean ± standard deviation. One-way analysis of variance was conducted using SPSS software (Statistical Package for the Social Sciences, version 19; SPSS Inc., Chicago, IL, USA), and Duncan's multiple range test was employed as a post-hoc test. The level of significance was set at $p < 0.05$.

3 Results

3.1 Morphological Characterizations

The SEM images in Fig. 2a show the presence of relatively large microscale Cu-doped TiO_2 nanoparticles produced using a high laser fluence on the outer surface. A higher resolution examination revealed the presence of interconnected Cu-doped TiO_2 NPs, which contributed to the substantially porous structure. Figure 2b shows that Cu-doped TiO_2 fabricated using a medium laser fluence formed on the porous structure. The well-developed porous UV-LIG shown in Fig. 2c, fabricated using a low laser fluence, exhibits interconnected TiO_2 NPs on the outer surface. Moreover, nanopores (< 1 nm) containing Cu-doped TiO_2 nanoparticles were formed.

3.2 Chemical Characterizations

Figure 3 shows the graphitic characteristics of the Cu-doped TiO_2/UV-LIG composites. Each sample was measured thrice to obtain their Raman spectra. The Raman spectrum of Cu-doped TiO_2/UV-LIG exhibits three major peaks. The D peak (I_D) appears at approximately 1330 cm^{-1}, indicating the presence of numerous defects or disorders. The G peak (I_G) at 1580 cm^{-1} represents the in-plane vibrational mode of sp^2 C atoms, whereas the 2D peak (I_{2D}) at 2700 cm^{-1} indicates a double resonance process involving two phonons [25–27]. The I_G peak broadened and shifted to lower wavenumbers, indicating defective graphene sheets with a significant number of edge sites and structural defects [27]. The I_{2D} peak also broadened and split into multiple peaks, suggesting the presence of multiple graphene layers [27–29]. The D and G peaks intensity ratio (I_D/I_G) is commonly used to gauge the degree of disorder or defects in the graphene lattice [28, 29]. The I_{2D}/I_G ratio also enables the assessment of the quality and structural properties, number of layers, and stacking order of graphene [13–15]. The I_{2D}/I_G intensity ratios for various graphene layers (> 4, triple, double, and single) were 0.07, 0.30, 0.8, and 1.6, respectively [30]. Table 1 lists the I_D/I_G and I_{2D}/I_G ratios and in-plane crystallite size (L_a) of the LIG samples derived from the Raman peaks. The I_D/I_G ratio and Raman excitation laser energy ($\lambda_1 = 532$ nm) can be used to determine L_a (Eq. (2)) [31, 32]:

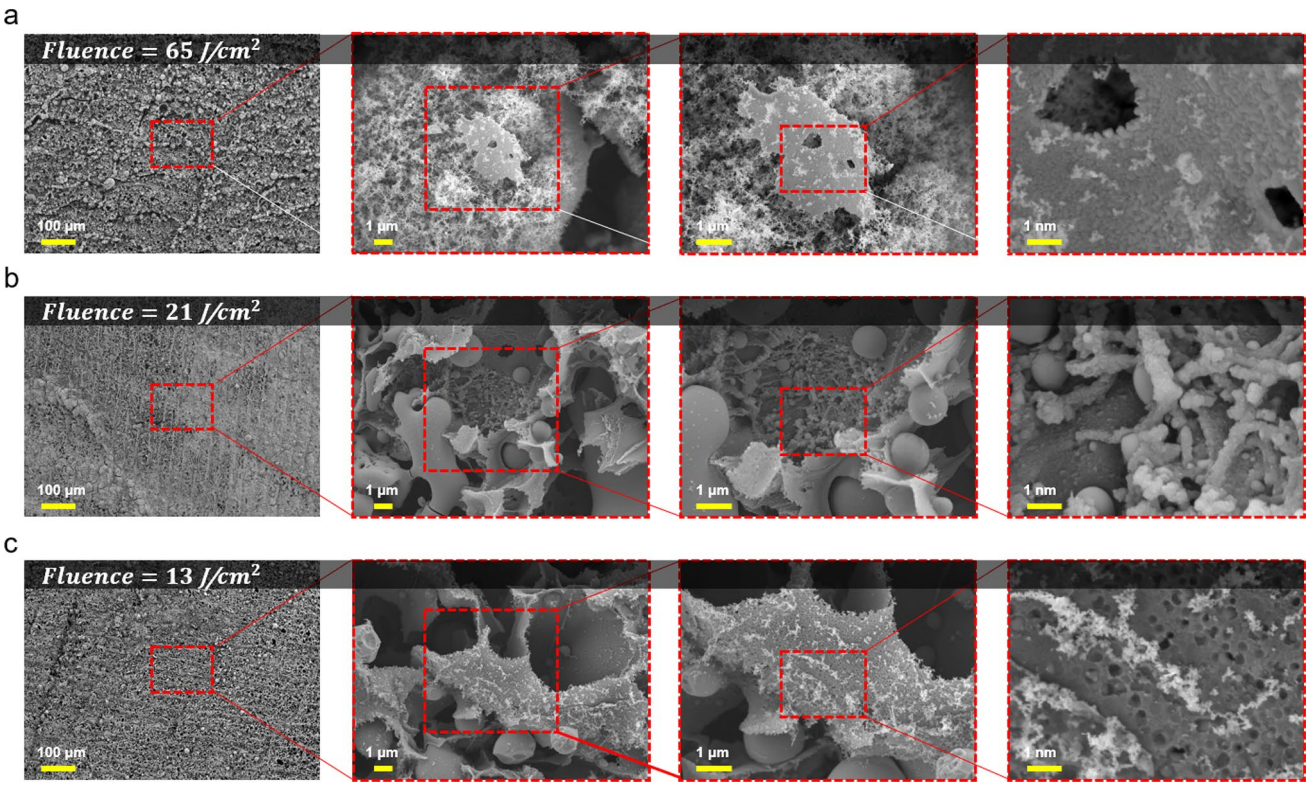

Fig. 2 FE-SEM images of Cu-doped TiO_2/UV-LIG prepared using **a** high, **b** medium, and **c** low laser fluence levels

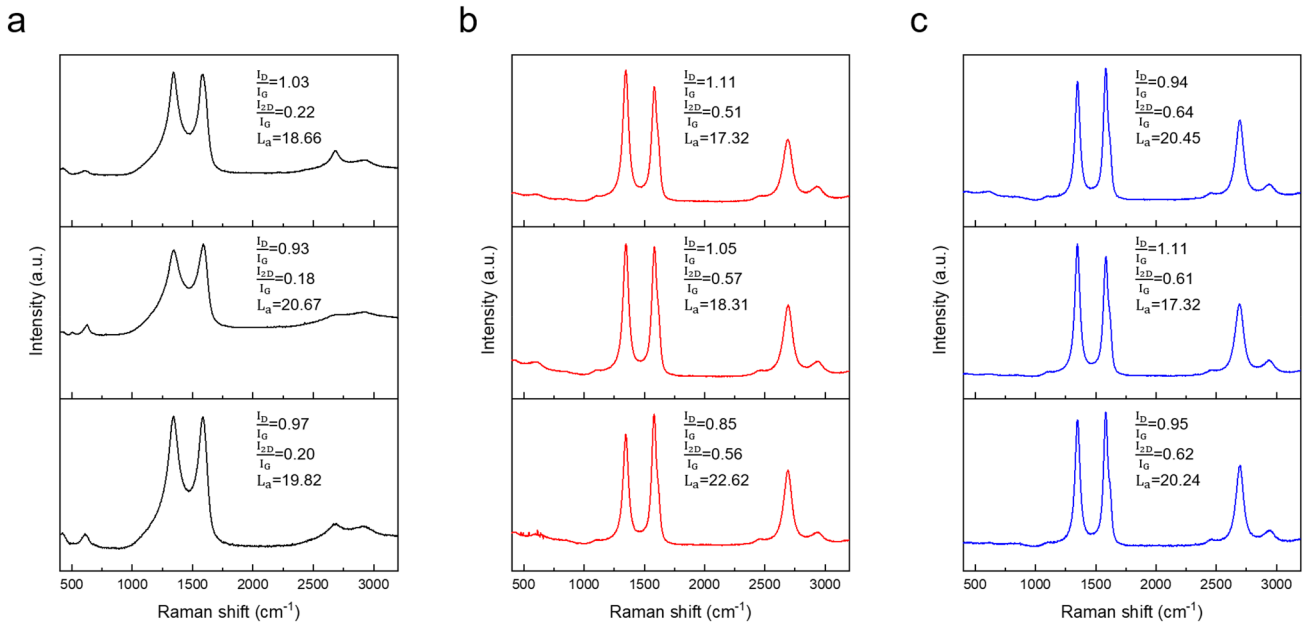

Fig. 3 Raman spectra of the Cu-doped TiO_2/UV-LIG samples fabricated using **a** high, **b** medium, and **c** low laser fluences

Table 1 Parameters obtained from the Raman spectra

Samples	I_D/I_G	I_{2D}/I_G	L_a(nm)
1. Cu-doped TiO_2/UV-LIG (High)	1.03	0.22	18.66
2. Cu-doped TiO_2/UV-LIG (High)	0.93	0.18	20.67
3. Cu-doped TiO_2/UV-LIG (High)	0.97	0.20	19.82
1. Cu-doped TiO_2/UV-LIG (Medium)	1.11	0.51	17.32
2. Cu-doped TiO_2/UV-LIG (Medium)	1.05	0.57	18.31
3. Cu-doped TiO_2/UV-LIG (Medium)	0.85	0.56	22.62
1. Cu-doped TiO_2/UV-LIG (Low)	0.94	0.64	20.45
2. Cu-doped TiO_2/UV-LIG (Low)	1.11	0.61	17.32
3. Cu-doped TiO_2/UV-LIG (Low)	0.95	0.62	20.24

I_D/I_G, I_{2D}/I_G, and L_a represent the intensity ratio of the D and G bands, intensity ratio of the 2D and G bands, and in-plane size of the graphitic crystallites, respectively

$$L_a(\mathrm{nm}) = \left(2.4 \times 10^{-10}\right)\lambda_1^4 \left(I_D/I_G\right)^{-1}. \quad (2)$$

Figure 4a–c respectively show the XPS C 1 s, Ti 2p, and Cu 2p spectra. The C 1 s XPS peak of graphene oxide in Fig. 4a exhibits distinct components at approximately 284.8 eV (C–C), 286 eV (C–O–C), and 288.5 eV (O–C=O), representing different C environments [13–15, 25]. The C–C peaks indicate the presence of sp^2-hybridized C atoms within the graphene lattice, while the C–O peaks indicate that C atoms bonded to O, which is characteristic of epoxide, hydroxyl, and carboxyl functional groups [13–15, 25]. The C=O component corresponds to carbonyl groups. The Ti 2p XPS spectrum in Fig. 4b exhibits the Ti $2p_{3/2}$ and Ti $2p_{1/2}$ binding energies at 459.15 and 464.85 eV, respectively, which was attributed to Ti^{4+} in TiO_2 [33, 34]. The high-resolution Cu 2p XPS data in Fig. 4c shows binding energies corresponding to CuO, with a dominant Cu 2p peak at approximately 934.7 eV (Cu $2p_{3/2}$ orbital) [35, 36]. Additionally, the spectrum exhibits a consistent satellite peak at a higher binding energy of approximately 945 eV. The Cu $2p_{1/2}$ peak appears at 954.7 eV [35, 36]. Figure 4 also presents the results of the Brunauer–Emmett–Teller (BET) surface area analyses, including the cumulative surface areas (Fig. 4d), cumulative volumes (Fig. 4e), and N_2 adsorption–desorption isotherms of the samples (Fig. 4f). The BET specific surface area was normalized and calculated using Eq. (3) [37]:

$$\frac{\frac{P}{P_0}}{V\left(1-\frac{P}{P_0}\right)} = \frac{1}{VmC} + \frac{C-1}{Vm} \times \frac{P}{P_0} \quad (3)$$

where P/P_0 is the relative pressure, Vm is the volume of the adsorbed gas (N_2), and C is the BET constant used to

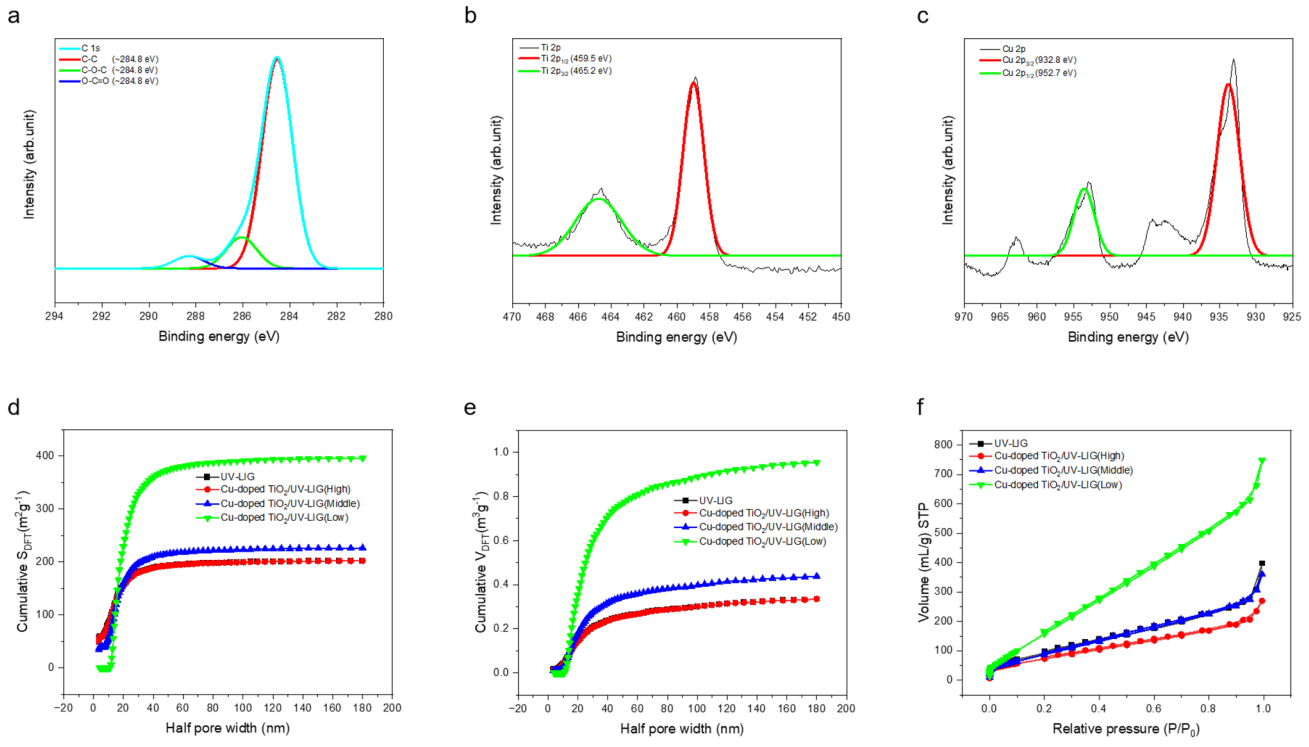

Fig. 4 XPS spectra of Cu-doped TiO_2/UV-LIG (Low): **a** C 1 s, **b** Ti 2p, and **c** Cu 2p. **d** Cumulative surface area, **e** cumulative volume, and **f** N_2 adsorption–desorption isotherms of the samples

Table 2 BET surface area, total pore volume, micropore volume, and average pore radii of the samples

Samples	Surface area (m^2 g^{-1})	Total pore volume (mL g^{-1})	Average pore radius (Å)
Cu-doped TiO_2/UV-LIG (Medium)	226.435	0.438	32.34
Cu-doped TiO_2/UV-LIG (Low)	396.071	0.954	31.62
Cu-doped TiO_2/UV-LIG (Medium)	226.435	0.438	32.34
UV-LIG	237.648	0.437	34.49

evaluate the volume change of the adsorbed gas relative to the pressure change. Table 2 lists the specific surface areas, total pore volumes, and average pore radii of the samples. The surface area increased with a decreasing dynamic fluence, with Cu-doped TiO_2/UV-LIG (Low) exhibiting the highest specific surface area of 396 m^2 g^{-1}.

3.3 Application of Cu-Doped TiO_2/UV-LIG for De-icing and Photodegradation

Graphene absorbs a significant proportion of incoming photons when exposed to sunlight, which leads to electronic excitation and heat generation (Fig. 5a). UV-LIG rapidly absorbs and distributes thermal energy when exposed to sunlight [18, 38]. TiO_2 NPs permeate into graphene in the presence of sunlight, thereby contributing to the photothermal effect. TiO_2 can also absorb UV light and, to a lesser extent, visible light, generating electron–hole pairs [39–41], which can be harnessed to prevent ice formation on surfaces. Moreover, TiO_2 NPs exhibit photocatalytic properties, allowing them to decompose organic contaminants upon exposure to light [39, 40, 42–44], as depicted in Fig. 5b. A self-cleaning surface is created when TiO_2 NPs are used in conjunction with UV-LIG. Figure 5c shows the hydrophobic functionality of UV-LIG, highlighting its water-repelling properties.

Figure 6a presents the temperature distribution of the Cu-doped TiO_2/UV-LIG samples under a 1 SUN illumination. Copper-doped TiO_2/UV-LIG (Low) exhibited a surface temperature of 93.1 °C at 1.1 SUN, demonstrating its remarkable photothermal properties. Figure 6b shows that the temperature of all the samples increased linearly from 0.5 to 1.1 SUN. Notably, UV-LIG exhibited the smallest temperature increase, confirming that the incorporation of Cu-doped TiO_2 NPs into UV-LIG significantly enhanced its

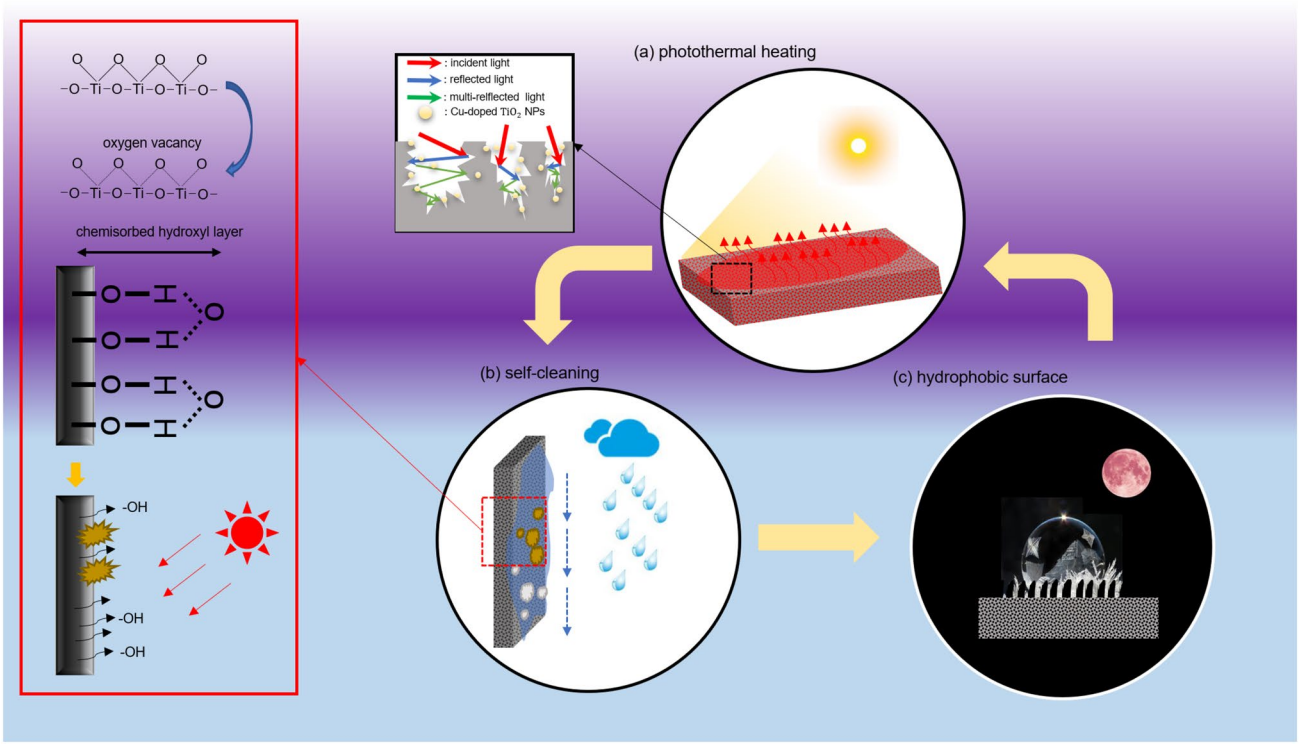

Fig. 5 Schematic diagram illustrating the functionalities of the multifunctional surface of Cu-doped TiO_2/UV-LIG in **a** photothermal heating and **b** self-cleaning, and **c** as a hydrophobic surface

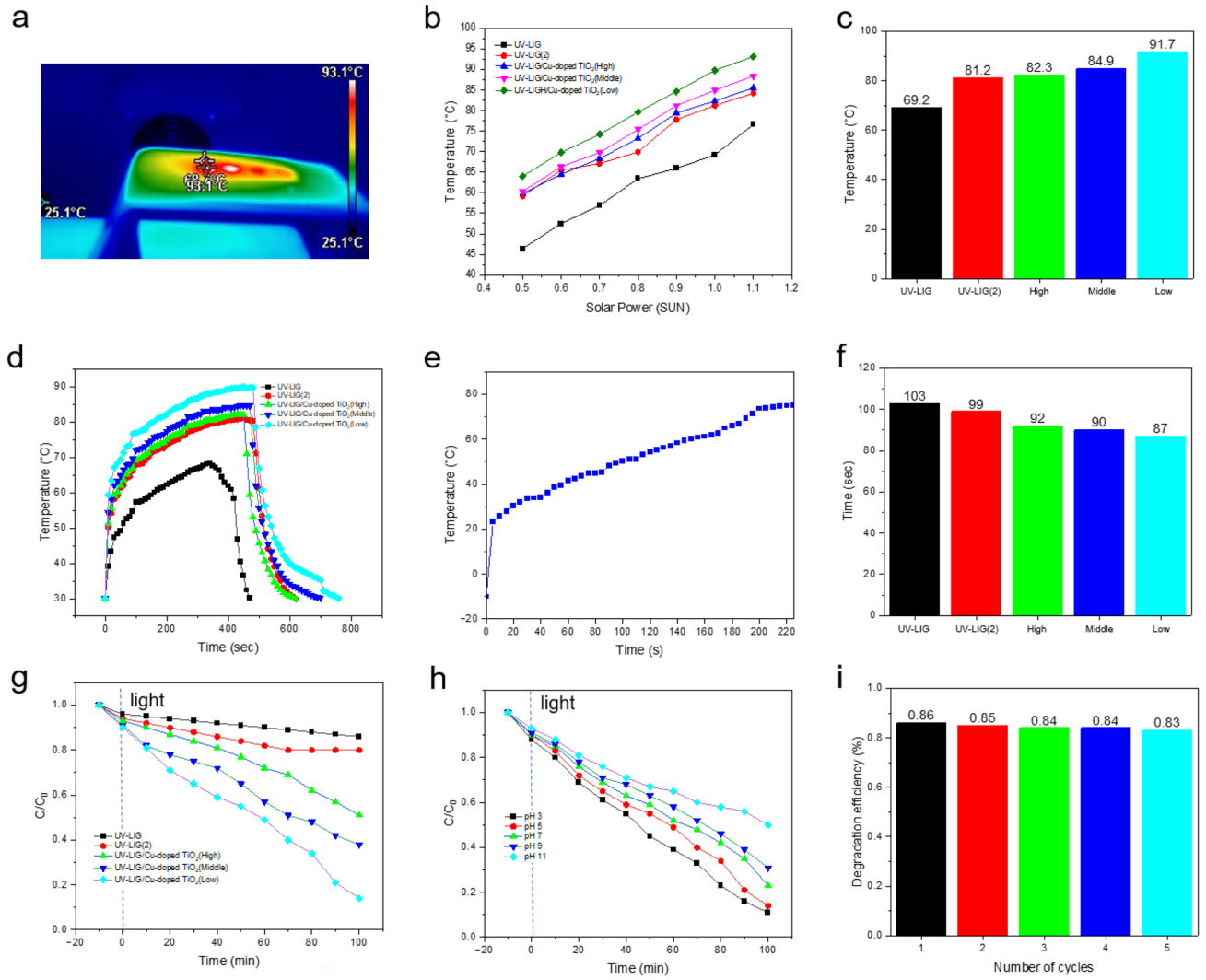

Fig. 6 **a** Thermal image showing the temperature gradient of the samples at 1 SUN, **b** temperature of the Cu-doped TiO_2/UV-LIG samples as a function of the solar power, **c** saturation temperatures at 1 SUN, **d** time required to reach the saturation temperature from the ambient temperature, **e** temperature change under 1 SUN with ice placed on the Cu-doped TiO_2/UV-LIG (Low) sample, **f** time taken to fully melt an ice column, **g** photodegradation of phenol, **h** dependence of photodegradation on pH, and **i** durability as a function of the number of cycles

photothermal conversion properties. Copper-doped TiO_2/UV-LIG (Low) exhibited the most substantial temperature increase, suggesting that the larger surface area of the Cu-doped TiO_2 NPs on the UV-LIG surface enhanced the photothermal conversion. Figure 6c shows the saturation temperature of the samples under a 1 SUN illumination. UV-LIG exhibits a conductive network with high surface area and thermal conductivity, and combining it with Cu-doped TiO_2 forms synergistic composites. Table S4 (Online Resource 1) lists the equilibrium temperature of the LIG and photothermal materials. Copper-doped TiO_2/UV-LIG (Low) achieved a temperature of 91.7 °C, representing the highest saturation temperature reported for LIG to date under 1 SUN irradiance. The heating and cooling times of the samples, defined as the time required to reach the maximum temperature at 1 SUN and that required to cool when the solar generator is turned off, respectively, were also compared (Fig. 6d). Because the temperature gradient changes in the samples were similar, comparable heating speeds were achieved. This observation indicates that UV-LIG containing Cu-doped TiO_2 NPs generate heat more efficiently through photothermal conversion than UV-LIG. Figure 6e shows the thermal response when a 5 mL ice mass was melted on a 1 cm × 1 cm Cu-doped TiO_2/UV-LIG (Low) sample under 1 SUN. Figure 6f shows the temporal evolution of the de-icing process achieved by affixing an ice column to the sample and inverting the assembly under a 1 SUN irradiation. Figure 6g shows the photodegradation of phenol under a 1 SUN

irradiation. Figure 6h shows the degradation behavior of Cu-doped TiO_2/UV-LIG (Low) as a function of pH, revealing that the photodegradation efficiency increased proportionally with a decreasing pH. Finally, Fig. 6i presents the efficiency profile as a function of the number of degradation cycles, highlighting the remarkable durability exhibited by the Cu-doped TiO_2/UV-LIG (Low) sample.

Figure 7a shows a thermal image of the excitation of electrons from the valence to the conduction band, generating electrons (e^-) and holes (h^+) as charge carriers. The combination of graphene with Cu-doped TiO_2 exhibits enhanced photocatalytic performance [44–46]; therefore, graphene can serve as a support material for Cu-doped TiO_2 NPs, increasing their stability and offering large surface areas for phenol adsorption. Additionally, graphene is an electron acceptor, facilitating the separation and transfer of photogenerated electrons from Cu-doped TiO_2. This prevents the recombination of electron–hole pairs, leading to an overall improvement in efficiency. Some of the photogenerated electrons reduce the O molecules (O_2) adsorbed on the Cu-doped TiO_2 surface, forming superoxide radicals ($O_2^{\bullet-}$) and hydrogen peroxide (H_2O_2), as depicted in Fig. 7b [43, 47]. These reactive oxygen species (ROS) and hydroxyl radicals ($^{\bullet}OH$) are produced when generated holes (h^+) react with water (H_2O). Hydroxyl radicals, being strong oxidizing agents [45], subsequently react with the adsorbed phenol molecules, breaking them down into less harmful compounds such as CO_2 and H_2O. Copper-doped TiO_2 combined with graphene enhances the photocatalytic properties of TiO_2 by leveraging the support and electron transport capabilities of graphene [44, 46]. This approach is efficient and environmentally friendly for the sunlight-induced degradation of organic pollutants, such as phenol, in water.

3.4 Enhanced Antibacterial Performance of Cu-Doped TiO_2/UV-LIG

The antibacterial efficacy of the Cu-doped TiO_2/UV-LIG composites produced using different laser fluences were compared. Tables 3 and 4 present the impact of Cu-doped TiO_2/UV-LIG on the foodborne pathogen (*B. cereus*, *S. typhimurium*, and *E. coli*) counts in 0.85% saline water. Notably, Cu-doped TiO_2/UV-LIG (Low) reduced the *B. cereus* and *S. typhimurium* counts to below the detection limit (1 log CFU/mL). The improved antibacterial performance of the Cu-doped TiO_2/UV-LIG (Low) composite films results from a synergistic combination of the factors illustrated in Fig. 8, including the sharp edges of graphene (Fig. 8a), photothermal heating (Fig. 8b), and photocatalysis for the generation of ROSs (Fig. 8c) [11, 12, 48, 49]. Various graphene sheets with inherent edges and defects are typically generated during the conventional production of LIG. However, our

Table 3 Change in the *B. cereus* counts in 0.85% saline water in response to treatments with various Cu-doped TiO_2/UV-LIG composites under 0.5 SUN illumination for 1 and 5 min

Treatment	*B. cereus* (log CFU/g)	
	1 min	5 min
Control	8.35 ± 0.06^{A}	8.35 ± 0.06^{A}
Cu-doped TiO_2 (High)	8.58 ± 0.03^{A}	7.67 ± 0.21^{B}
Cu-doped TiO_2 (Medium)	6.24 ± 0.10^{D}	N.D
Cu-doped TiO_2 (Low)	N.D	N.D

Control: No treatment. Values represent the mean ± SD

N.D. not detected or below the detection limit (1 log CFU/mL)

Duncan multiple range tests ($p < 0.05$) indicated that the mean values in the same column (a–c) followed by different letters were significantly different

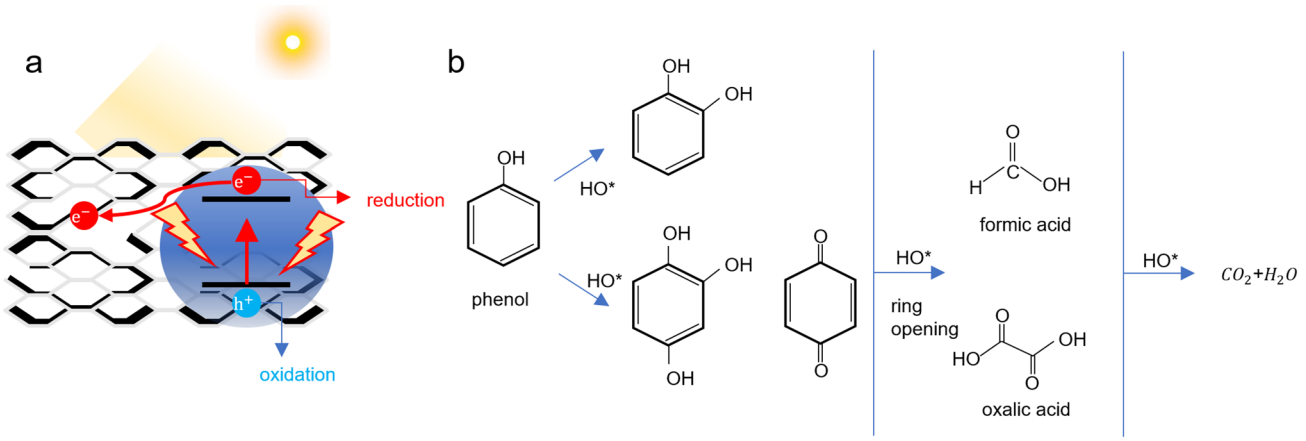

Fig. 7 **a** Schematic diagram illustrating the photodegradation mechanism and **b** chemical path for the decomposition of phenol by hydroxyl radicals ($^{\bullet}OH$)

Table 4 Change in the *B. cereus*, *S. typhimurium*, and *E. coli* counts in 0.85% saline water in response to treatments with UV-LIG in combination with Cu-doped TiO_2 under 0.5 SUN illumination for 1 min

Treatment	Foodborne pathogen (log CFU/g)		
	B. cereus	*S. typhimurium*	*E. coli*
Control	8.19 ± 0.14^{A}	9.15 ± 0.09^{A}	8.97 ± 0.01^{A}
Cu-doped TiO_2 (High)	8.58 ± 0.03^{A}	8.26 ± 0.14^{B}	8.53 ± 0.05^{BCD}
Cu-doped TiO_2 (Medium)	7.34 ± 0.09^{DE}	N.D	8.25 ± 0.28^{E}
Cu-doped TiO_2 (Low)	N.D	N.D	N.D

Control: No treatment. Values represent the mean ± SD

N.D. not detected or below the detection limit (1 log CFU/mL)

Duncan multiple range tests ($p < 0.05$) indicated that the mean values in the same column (a–c) followed by different letters were significantly different

specific manufacturing approach augments the quantity of graphene edges and defects on the high-surface area LIG by synthesizing Cu-doped TiO_2 NPs using a UV pulsed laser [7, 50]. The integration of Cu-doped TiO_2 nanoparticles within the graphene sheets increased exfoliation, which yielded a notably irregular surface with abundant sharp graphene edges. The sharp edges of graphene within the Cu-doped TiO_2/UV-LIG contributes to its physical interaction with the bacterial cells, which damages the bacterial cell membranes, compromising their structural integrity and increasing their permeability [48, 51–53]. This direct mechanical disruption is particularly effective at weakening bacterial cells, making them more susceptible to other antimicrobial mechanisms [7, 49, 50]. The edges of Cu-doped TiO_2/UV-LIG (Low), characterized by its extensive surface area, harbor numerous active sites that facilitate interaction with bacteria, thus increasing susceptibility to various antimicrobial mechanisms such as photo-induced thermal heating and ROSs. This phenomenon is evidenced by its non-detectable (N.D.) bacterial count within 1 min, as elucidated in Table 3. In contrast, Cu-doped TiO_2/UV-LIG (High), possessing a relatively diminished surface area, did not substantially reduce the *B. cereus* count (7.67 ± 0.21 log CFU/g) even after 5 min despite the concurrent effects of the photothermal activity and ROS generation. The bacterial experiments involving *S. typhimurium* and *E. coli* exhibited a similar trend. As shown in Table 4, Cu-doped TiO_2/UV-LIG (Low), distinguished by a substantial abundance of edges attributable to its large surface area, achieved N.D. levels within 1 min of 0.5 SUN irradiation. In contrast, Cu-doped TiO_2/UV-LIG (High), characterized by a relatively reduced surface area with fewer edges, demonstrated a lower reduction, as compared to the control group.

Cu-doped TiO_2 can generate highly reactive ROSs, such as $^{\bullet}OH$ and $O_2^{\bullet-}$, that cause oxidative damage to bacterial cell components, including lipids, proteins, and DNA, as shown in Fig. 8c [19, 20]. Copper-doped TiO_2 NPs, incorporating Cu_2O (with a bandgap of 2.2 eV), TiO_2 in its anatase phase (with a bandgap of 3.2 eV), TiO_2 in its rutile phase (with a bandgap of 3 eV), and CuO (with a bandgap of 1.7 eV), demonstrated considerable potential as an antibacterial photocatalyst [54, 55].

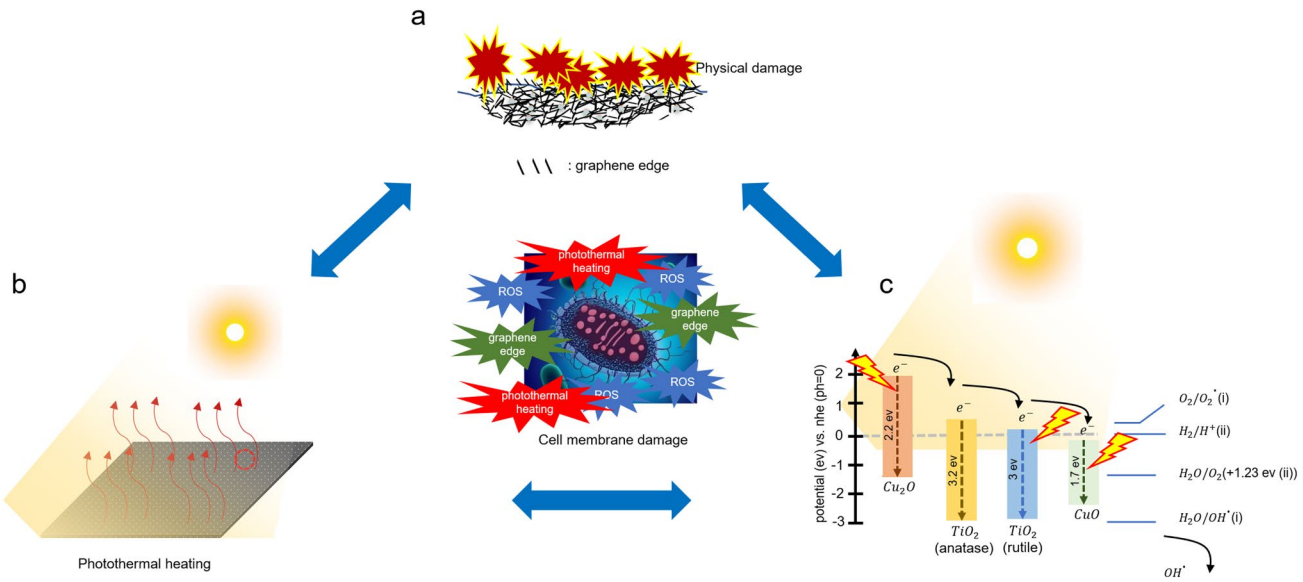

Fig. 8 Enhanced antibacterial performance obtained through **a** the sharp edges of graphene, **b** photothermal heating, and **c** photocatalytic generation of antibacterial ROS

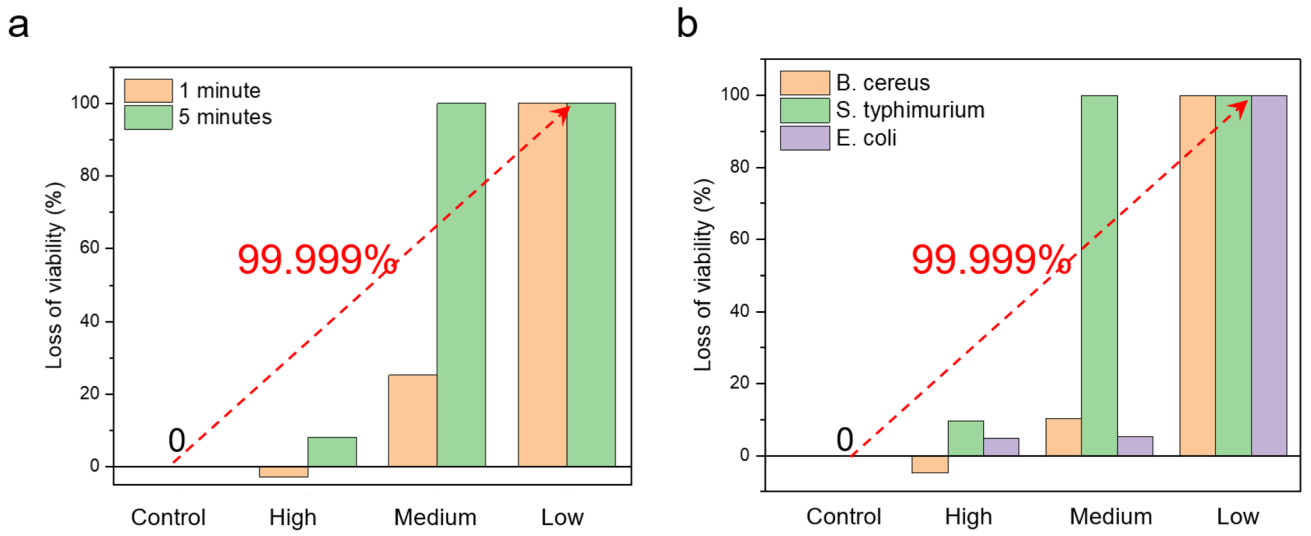

Fig. 9 **a** loss of viability measured for *B. cereus* under 0.5 SUN for 1 min and 5 min, **b** loss of viability measured for *B. cereus, S. typhimurium* and *E. coli* under 0.5 SUN for 1 min

The sharp graphene edges, localized photothermal heating, and photocatalytic ROS generation of the composite film collectively establish an inhospitable setting for bacteria. This multifaceted strategy ensures a more comprehensive and effective antibacterial performance than the individual mechanisms. This synergy enables the composite film to target bacteria through both physical disruption and oxidative stress, making it a robust and efficient antibacterial material. The intricate interplay of antibacterial properties renders the exact mechanism of bacterial death elusive. Therefore, a thorough investigation into the mechanism of cellular demise becomes imperative, particularly in scenarios involving repeated utilization. Figure 9 shows the loss of viability measured for foodborne pathogens, demonstrating that the Cu-doped TiO_2-UV-LIG coating is bactericidal. Its excellent antibacterial performance shows a 99.999% increase in bacteria killing for a variety of foodborne pathogens.

4 Conclusion

The versatility of Cu-doped TiO_2/UV-LIG under solar radiation is under scrutiny for diverse applications such as photodegradation and antibacterial efficacy.

(1) With nanopores and a surface area of 396 m^2/g, Cu-doped TiO_2/UV-LIG (Low) achieved a groundbreaking temperature of 91.7 °C under 1 SUN irradiance, setting a new benchmark in LIG.
(2) Initially, it showed outstanding phenol degradation efficiency at 86%, maintaining a remarkable 83% even after five uses, highlighting its exceptional degradation capability.
(3) At 0.5 SUN intensity, it effectively eliminated over 99.999% of foodborne pathogens including B. cereus and S. typhimurium.

These nanocomposites hold substantial promise for applications spanning water purification, air filtration, and medical devices.

Supplementary Information The online version contains supplementary material available at https://doi.org/10.1007/s40684-024-00653-5.

Acknowledgements This research was supported by a grant of the Korea Health Technology R&D Project through the Korea Health Industry Development Institute (KHIDI), funded by the Ministry of Health &Welfare, Republic of Korea (grant number : HI19C1085) and the Natural Sciences and Engineering Research Council of Canada (NSERC) under Discovery Grant RGPIN-2019-05778.

Author Contributions Methodology, J.U.L., B.-S.K. and Y.-W.M.; software, J.U.L.; and B.-S.K.; validation, J.U.L. and Y.-W.M.; formal analysis, J.U.L.; R.A and B.-S.K.; investigation, J.U.L., B.-S.S. and Y.-W.M.; resources, J.U.L. and P.C.L.; data curation, J.U.L.; B.-S.K. and Y.-W.M.; writing—original draft preparation, J.U.L., B.-S.K. and Y.-W.M.; writing—review and editing, R.A, P.C.L. and B.-S.S.; visualization, J.U.L., P.C.L.; supervision, P.C.L, B.-S.S.; project administration, P.C.L.; B.-S.S.; funding acquisition, P.C.L.; B.-S.S. All authors have read and agreed to the published version of the manuscript.

Funding Natural Sciences and Engineering Research Council of Canada, RGPIN-2019-05778, Patrick Lee.

Data Availability The data presented in this study are available on request from the corresponding author.

Declarations

Conflict of Interest The authors declare no conflicts of interest.

References

1. Mondal, A., Prabhakaran, A., Gupta, S., & Subramanian, V. R. (2021). Boosting photocatalytic activity using reduced graphene oxide (RGO)/semiconductor nanocomposites: Issues and future scope. *ACS Omega, 6*(13), 8734–8743.
2. Serpone, N. A. V. E., & Emeline, A. V. (2012). Semiconductor Photocatalysis past, present, and future outlook. *Journal of Physical Chemistry Letters, 3*(5), 673–677.
3. Kisch, H. (2013). Semiconductor photocatalysis—mechanistic and synthetic aspects. *Angewandte Chemie International Edition, 52*(3), 812–847.
4. Wang, H., Zhang, L., Chen, Z., Hu, J., Li, S., Wang, Z., Liu, J., & Wang, X. (2014). Semiconductor heterojunction photocatalysts: Design, construction, and photocatalytic performances. *Chemical Society Reviews, 43*(15), 5234–5244.
5. Kamat, P. V., & Jin, S. (2018). Semiconductor photocatalysis:"tell us the complete story!" *ACS Energy Letters, 3*(3), 622–623.
6. Ye, R., James, D. K., & Tour, J. M. (2018). Laser-induced graphene. *Accounts of Chemical Research, 51*(7), 1609–1620.
7. Lee, J., Lee, J., Lee, C., Cho, S., Hong, S., Ma, Y., Jeong, S., & Shin, B. (2022). Green synthesis of laser-induced graphene with copper oxide nanoparticles for deicing based on photo-electrothermal effect. *Nanomaterials, 12*(6), 960.
8. Zhao, J., Yi, N., Ding, X., Liu, S., Zhu, J., Castonguay, A. C., Gao, Y., Zarzar, L. D., & Cheng, H. (2023). In situ laser-assisted synthesis and patterning of graphene foam composites as a flexible gas sensing platform. *Journal of Chemical Engineering, 456*(15), 140956.
9. Zhu, C., Dong, X., Mei, X., Gao, M., Wang, K., & Zhao, D. (2021). General fabrication of metal oxide nanoparticles modified graphene for supercapacitors by laser ablation. *Applied Surface Science, 568*(1), 150978.
10. Sharma, C. P., & Arnusch, C. J. (2022). Laser-induced graphene composite adhesive tape with electro-photo-thermal heating and antimicrobial capabilities. *Carbon, 196*, 102–109.
11. Huang, L., Xu, S., Wang, Z., Xue, K., Su, J., Song, Y., Chen, S., Zhu, C., Tang, B. Z., & Ye, R. (2020). Self-reporting and photothermally enhanced rapid bacterial killing on a laser-induced graphene mask. *ACS Nano, 14*(9), 12045–12053.
12. Pal, K., Jr., Kyzas, G. Z., Kralj, S., & Gomes de Souza, F. (2021). Sunlight sterilized, recyclable and super hydrophobic anti-COVID laser-induced graphene mask formulation for indelible usability. *Journal of Molecular Structure, 1233*, 130100.
13. Wang, D., Li, J., Wang, Y., Liu, F., Wang, G., Ding, X., Luo, S., & Chen, G. (2022). Laser-induced graphene papers with tunable microstructures as antibacterial agents. *ACS Applied Nano Materials, 5*(5), 6841–6851.
14. Zhu, S., Lei, Z., Dou, Y., Lou, C.-W., Lin, J.-H., & Li, J. (2023). Sputter-deposited nickel nanoparticles on Kevlar fabrics with laser-induced graphene for efficient solar evaporation. *Chemical Engineering Journal, 452*(4), 139403.
15. Gu, M., Huang, L., Wang, Z., Guo, W., Cheng, L., Yuan, Y., Zhou, Z., Hu, L., Chen, S., Shen, C., Tang, B. Z., & Ye, R. (2021). Molecular engineering of laser-induced graphene for potential-driven broad-spectrum antimicrobial and antiviral applications. *Small (Weinheim an der Bergstrasse, Germany), 17*(51), 2102841.
16. Chen, Y., Long, J., Xie, B., Kuang, Y., Chen, X., Hou, M., Gao, J., Liu, H., He, Y., & Wong, C.-P. (2022). One-step ultraviolet laser-induced fluorine-doped graphene achieving superhydrophobic properties and its application in deicing. *ACS Applied Materials & Interfaces, 14*(3), 4647–4655.
17. Lim, H., Kwon, H., Kang, H., Jang, J. E., & Kwon, H.-J. (2023). Semiconducting MOFs on ultraviolet laser-induced graphene with a hierarchical pore architecture for NO_2 monitoring. *Nature Communications, 14*(1), 3114.
18. Lee, J.-U., Lee, C.-W., Cho, S.-C., & Shin, B.-S. (2021). Laser-induced graphene heater pad for de-icing. *Nanomaterials, 11*(11), 3093.
19. Yuzer, B., Aydın, M. I., Con, A. H., Inan, H., Can, S., Selcuk, H., & Kadmi, Y. (2022). Photocatalytic, self-cleaning and antibacterial properties of Cu(II) doped TiO_2. *Journal of Environmental Management, 302*(Part A), 114023.
20. Lu, S., Li, R., Chai, M., Wang, J., Duan, W., Yao, X., Zhang, X., & Tang, B. (2022). Nanostructured Cu-doped TiO_2 with photothermal effect for prevention of implant-associated infection. *Colloids and Surfaces. B, Biointerfaces, 217*, 112695.
21. Zhou, X. M., Zou, T. S., & Chen, R. (2020). Sunlight-triggered dye degradation and antibacterial activity of graphene-iron oxide-titanium dioxide heterostructure nanocomposites. *Journal of Nanoscience and Nanotechnology, 20*(7), 4158–4162.
22. Guo, M. T., & Tian, X. B. (2019). Impacts on antibiotic-resistant bacteria and their horizontal gene transfer by graphene-based TiO_2 & Ag composite photocatalysts under solar irradiation. *Journal of Hazardous Materials, 380*, 120877.
23. Song, S., Um, S.-H., Park, J., Ha, I., Lee, J., Kim, S., Lee, H., Cheon, C.-H., Ko, S. H., Kim, Y.-C., & Jeon, H. (2022). Rapid synthesis of multifunctional apatite via the laser-induced hydrothermal process. *ACS Nano, 16*(8), 12840–12851.
24. Yeo, J., Hong, S., Kim, G., Lee, H., Suh, Y. D., Park, I., Grigoropoulos, C. P., & Ko, S. H. (2015). Laser-induced hydrothermal growth of heterogeneous metal-oxide nanowire on flexible substrate by laser absorption layer design. *ACS Nano, 9*(6), 6059–6068.
25. Lin, J., Peng, Z., Liu, Y., Ruiz-Zepeda, F., Ye, R., Samuel, E. L. G., Yacaman, M. J., Yakobson, B. I., & Tour, J. M. (2014). Laser-induced porous graphene films from commercial polymers. *Nature Communications, 5*, 5714.
26. Chyan, Y., Ye, R., Li, Y., Singh, S. P., Arnusch, C. J., & Tour, J. M. (2018). Laser-induced graphene by multiple lasing: toward electronics on cloth, paper, and food. *ACS Nano, 12*(3), 2176–2183.
27. Ferrari, A. C., Meyer, J. C., Scardaci, V., Casiraghi, C., Lazzeri, M., Mauri, F., Piscanec, S., Jiang, D., Novoselov, K. S., Roth, S., & Geim, A. K. (2006). Raman spectrum of graphene and graphene layers. *Physical Review Letters, 97*(18), 187401.
28. Wróblewska, A., Dużyńska, A., Judek, J., Stobiński, L., Żerańska, K., Gertych, A. P., & Zdrojek, M. (2017). Statistical analysis of the reduction process of graphene oxide probed by Raman spectroscopy mapping. *Journal of Physics: Condensed Matter, 29*(47), 475201.
29. Scardaci, V., & Compagnini, G. (2021). Raman spectroscopy data related to the laser induced reduction of graphene oxide. *Data in Brief, 38*, 107306.
30. Akhavan, O., Ghaderi, E., Hashemi, E., & Rahighi, R. (2014). Ultra-sensitive detection of leukemia by graphene. *Nanoscale, 6*(24), 14810–14819.
31. Maslova, O., Ammar, M.-R., Guimbretière, G., Rouzaud, J. N., & Simon, P. (2012). Determination of crystallite size in polished graphitized carbon by Raman spectroscopy. *Physical Reviews B, 86*(13), 134205.
32. Cançado, L. G., Jorio, A., & Pimenta, M. A. (2007). Measuring the absolute Raman cross section of nanographites as a function of laser energy and crystallite size. *Physical Reviews B, 76*(6), 064304.
33. Li, W., Yang, X., Fu, H., An, X., & Zhao, H. (2019). Synthesis of TiO_2-Reduced graphene oxide nanocomposites offering highly enhanced photocatalytic activity. *Journal of Nanoscience and Nanotechnology, 19*(11), 7089–7096.
34. Rtimi, S., Nesic, J., Pulgarin, C., Sanjines, R., Bensimon, M., & Kiwi, J. (2015). Effect of surface pretreatment of TiO_2 films on

interfacial processes leading to bacterial inactivation in the dark and under light irradiation. *Interface Focus, 5*(1), 20140046.
35. Lee, J. U., Kang, B. S., Cho, S. C., Shin, B. S., & Lee, P. C. (2024). Facile Fabrication of highly flexible and sensitive strain sensors based on UV-laser-reduced graphene oxide with CuO nanoparticles for human health monitoring. *International Journal of Precision Engineering and Manufacturing-Green Technology*. https://doi.org/10.1007/s40684-024-00632-w.
36. Cuong, H. N., Pansambal, S., Ghotekar, S., Oza, R., Hai, N. T. T., Viet, N. M., & Nguyen, V. H. (2022). New frontiers in the plant extract mediated biosynthesis of copper oxide (CuO) nanoparticles and their potential applications: A review. *Environmental Research, 203*, 111858.
37. Zhang, S., Wang, H., Liu, J., & Bao, C. (2020). Measuring the specific surface area of monolayer graphene oxide in water. *Materials Letters, 261*(15), 127098.
38. Jiao, Z.-Z., Zhou, H., Han, X.-C., Han, D.-D., & Zhang, Y.-L. (2023). Photothermal responsive slippery surfaces based on laser-structured graphene@PVDF composites. *Journal of Colloid and Interface Science, 629*(Part A), 582–592.
39. Kanakaraju, D., Motti, C. A., Glass, B. D., & Oelgemöller, M. (2015). TiO_2 photocatalysis of naproxen: Effect of the water matrix, anions and diclofenac on degradation rates. *Chemosphere, 139*, 579–588.
40. Pereira, L., Pereira, R., Oliveira, C. S., Apostol, L., Gavrilescu, M., Pons, M.-N., Zahraa, O., & Alves, M. M. (2013). UV/TiO_2 photocatalytic degradation of xanthene dyes. *Photochemistry and Photobiology, 89*(1), 33–39.
41. Ren, W., Yan, Y., Zeng, L., Shi, Z., Gong, A., Schaaf, P., Wang, D., Zhao, J., Zou, B., Yu, H., Chen, G., Brown, E. M. B., & Wu, A. (2015). A Near infrared light triggered hydrogenated black TiO_2 for cancer photothermal therapy. *Advanced Healthcare Materials, 4*(10), 1526–1536.
42. Akhavan, O., & Ghaderi, E. (2013). Differentiation of human neural stem cells into neural networks on graphene nanogrids. *Journal of Materials Chemistry. B, 1*(45), 6291–6301.
43. Lee, H.-G., Sai-Anand, G., Komathi, S., Gopalan, A.-I., Kang, S.-W., & Lee, K.-P. (2015). Efficient visible-light-driven photocatalytic degradation of nitrophenol by using graphene-encapsulated TiO_2 nanowires. *Journal of Hazardous Materials, 283*, 400–409.
44. Morales-Torres, S., Pastrana-Martínez, L. M., Figueiredo, J. L., Faria, J. L., & Silva, A. M. T. (2012). Design of graphene-based TiO_2 photocatalysts-a Review. *Environmental Science and Pollution Research International, 19*(9), 3676–3687.
45. Sharma, A., & Lee, B.-K. (2016). Rapid photo-degradation of 2-chlorophenol under visible light irradiation using cobalt oxide-loaded TiO_2/reduced graphene oxide nanocomposite from aqueous media. *Journal of Environmental Management, 165*, 1–10.
46. Yang, N., et al. (2012). Granum-like stacking structures with TiO2 -graphene nanosheets for improving photo-electric conversion. *Small (Weinheim an der Bergstrasse, Germany), 8*(11), 1762–1770.
47. Zhang, H., Guo, L.-H., Wang, D., Zhao, L., & Wan, B. (2015). Light-induced efficient molecular oxygen activation on a Cu(II)-grafted TiO_2/graphene photocatalyst for phenol degradation. *ACS Applied Materials & Interfaces, 7*(3), 1816–1823.
48. Zhou, H., Zou, F., Koh, K., & Lee, J. (2022). Antibacterial activity of graphene-based nanomaterials. In D. W. Han & S. W. Hong (Eds.), *Multifaceted biomedical applications of graphene* (pp. 233–250). Springer.
49. Cao, G., Yan, J., Ning, X., Zhang, Q., Wu, Q., Bi, L., Zhang, Y., Han, Y., & Guo, J. (2021). Antibacterial and antibiofilm properties of graphene and its derivatives. *Colloids and Surfaces. B, Biointerfaces, 200*, 111588.
50. Thirumalai, D., Lee, J.-U., Choi, H., Kim, M., Lee, J., Kim, S., Shin, B.-S., & Chang, S.-C. (2020). In situ synthesis of copper–ruthenium bimetallic nanoparticles on laser-induced graphene as a peroxidase mimic. *Chemical Communications, 57*, 1947–1950.
51. Singh, S. P., Li, Y., Be'er, A., Oren, Y., Tour, J. M., & Arnusch, C. J. (2017). Laser-induced graphene layers and electrodes prevents microbial fouling and exerts antimicrobial action. *ACS Applied Materials & Interfaces, 9*(21), 18238–18247.
52. Pandit, S., Gaska, K., Mokkapati, V. R. S. S., Celauro, E., Derouiche, A., Forsberg, S., Svensson, M., Kádár, R., & Mijakovic, I. (2020). Precontrolled alignment of graphite nanoplatelets in polymeric composites prevents bacterial attachment. *Small (Weinheim an der Bergstrasse, Germany), 16*(5), e1904756.
53. Pandit, S., Cao, Z., Mokkapati, V. R. S. S., Celauro, E., Yurgens, A., Lovmar, M., Westerlund, F., Sun, J., & Mijakovic, I. (2018). Vertically aligned graphene coating is bactericidal and prevents the formation of bacterial biofilms. *Advanced Materials Interfaces, 5*(7), 1701331.
54. Mathew, S., Ganguly, P., Rhatigan, S., Kumaravel, V., Byrne, C., Hinder, S. J., Bartlett, J., Nolan, M., & Pillai, S. C. (2018). Cu-doped TiO2: Visible light assisted photocatalytic antimicrobial activity. *Applied Sciences, 8*(11), 2067.
55. Pedroza-Herrera, G., Medina-Ramírez, I. E., Lozano-Álvarez, J. A., & Rodil, S. E. (2020). Evaluation of the photocatalytic activity of copper doped TiO_2 nanoparticles for the purification and/or disinfection of industrial effluents. *Catalysis Today, 341*(1), 37–48.

Jun Uk Lee is presently serving as a Postdoctoral Fellow in the Multifunctional Composites Manufacturing Laboratory (MCML) at the University of Toronto. He earned his Ph.D. degree from Pusan National University, Busan, Republic of Korea, in 2023. His research focuses on the development of innovative manufacturing processes utilizing lasers and bio-inspired hybrid composites, as well as micro-/nano-layer structuring.

Bo-Seok Kang is a graduate of the Engineering Research Center for Net Shape and die Manufacturing at Busan National University in Korea with a master's degree. Currently, he has completed a doctoral course in Department of Cogno-Mechartronics Engineering at Busan National University. Currently, he is mainly studying laser processing and selective permeation films using polymers.

Yong-Won Ma received his Ph.D. in mechanical engineering, specializing in laser processing, from Pusan National University. His expertise includes laser-based micro/nanofabrication systems, with significant contributions to periodic/nonperiodic nanopatterning, additive manufacturing, material-decorated processing, and material transformation. Currently, he is a researcher at the Korea Research Institute of Decommissioning (KRID), where he focuses on nuclear power plant decommissioning. His work at KRID encompasses laser-based cutting, decontamination, and the application of advanced robotic technologies.

Rafaela Aguiar is a Postdoctoral Fellow at the Multifunctional Composites Manufacturing Laboratory (MCML) within the Department of Mechanical and Industrial Engineering at the University of Toronto. She holds a Ph.D. in Mechanical Engineering from Carleton University. Her current research focuses on lightweight, high-strength biomimetic hierarchical hybrid composites. These materials are specifically tailored for demanding applications across the automotive, aerospace, military, and defense sectors. Dr. Aguiar also explores high-value applications for biodegradable polymers, seeking solutions to create high-performance materials with superior mechanical, electrical, thermal, gas barrier, and biological properties.

Bo-Sung Shin received the Ph.D. in mechanical engineering from the Korea Advanced Institute of Science and Technology (KAIST). After being with Department of Ordnance Engineering in Korea Military Academy as a Full-time professor for 3 years, he joined Korea institute of machinery & materials (KIMM) as a director in the Nano process group. Since 2012, he has been a lecturer in the Department of Optics and Mechatronics Engineering at the Pusan National University, Pusan, Republic of Korea. His work primarily involves finite element modelling of magnetic and mechanical systems, and laser processing system design.

Patrick C. Lee PhD, PEng is an Associate Professor in the Department of Mechanical & Industrial Engineering (MIE) at the University of Toronto. He received his B.Sc. degree in Mechanical Engineering from the University of British Columbia, and then obtained his M.A.Sc. and Ph.D. in Mechanical Engineering from the University of Toronto in 2001 and 2006, respectively. Then he pursued Postdoctoral study in the Department of Chemical Engineering and Materials Science at the University of Minnesota. Dr. Lee began his professional career at The Dow Chemical Company in 2008. He was a Research Scientist and Project Leader in Dow's Research and Development organization. Dr. Lee joined the Department of Mechanical Engineering at The University of Vermont as an assistant professor in 2014. Since joining UVM, he created his own research platform on the lightweight and smart composite structures. He joined the Department of Mechanical and Industrial Engineering at The University of Toronto starting July 1st, 2018. Dr. Lee's research areas focus on polymer foam processing and characterization, and processing-structure-property relationships of nano-composites. He has 61 journal papers, over 100 refereed conference abstracts/papers, 2 book chapters, and 20 filed/issued patent applications. He is the PI or co-PI on domestically and internationally awarded grants from various government agencies and industries. Among his honors, Dr. Lee received the G.H. Duggan Medal from Canadian Society for Mechanical Engineering (CSME) in 2020, the AKCSE Early Achievement Award in 2019, the US National Science Foundation Early Faculty Career Development Award (NSF CAREER) in 2018, the Polymer Processing Society (PPS) Morand Lambla award in 2018, the Hanwha Advanced Materials Non-Tenured Faculty Award in 2017, and 3 best paper awards from the Society of Plastics Engineer (2005, 2 in 2011).